JOURNAL OF COLLOID AND INTERFACE SCIENCE **187,** 243–258 (1997)
ARTICLE NO. CS964711

Simulation of Coating Layer Evolution and Drop Formation on Horizontal Cylinders

DAVID E. WEIDNER, LEONARD W. SCHWARTZ,[1] AND MURAT H. ERES

Department of Mechanical Engineering, University of Delaware, Newark, Delaware 19716

Received August 9, 1996; accepted November 19, 1996

The lubrication form of the equations governing the flow of a thin liquid film on a horizontal right circular cylinder is derived. The equations are discretized and solved numerically using an alternating-direction implicit algorithm. Simulations demonstrate that the transition from a uniform coating to a final configuration of distinct drops follows a similar evolution for a wide range of cylinder radii. Initially gravity-driven drainage from the top and sides of the cylinder dampens the formation of any axial disturbances; only when this drainage slows do longitudinal waves begin to develop along the bottom of the cylinder. These waves grow rapidly and a series of alternating primary and satellite drops form during the transition from a linear to a nonlinear wave growth regime. This is followed by a slow drainage between adjacent drops as the drop pattern approaches an equilibrium state where surface tension forces exactly balance gravitational forces in each discrete drop. For large cylinder radii, these drops are localized on the bottom of the cylinder, while, for sufficiently small cylinder radii, these drops may wrap around the entire circumference of the cylinder. Integral measures of the evolving coating profile, such as the total energy and viscous dissipation rate, clearly show these growth phases. The equilibrium shape of large-amplitude pendant drops and the maximum sustainable drop volume for various cylinders are also considered.

Key Words: **coating flows; drop formation; three-dimensional simulation; curved substrates.**

I. INTRODUCTION

The motion of a liquid film under the combined influence of surface tension, gravitational, and viscous forces has received much attention in the fluid mechanics literature. Such films occur in many industrial applications, such as the coating of objects with paint films and many heat transfer problems, as well as natural phenomena, such as the coating of the alveoli of the lungs with a thin mucous film. In addition, the wave motion and pattern formation occurring in such films has been a subject of much interest to the physics community.

Much of the work has concentrated on the canonical problem of a liquid film flowing down an inclined plane (1, 2), but the coating of cylindrical objects has also been addressed. Rayleigh considered the capillary instability of a cylindrical liquid jet and found that longitudinal waves with wavelengths greater than the circumference will grow, and those with wavelengths less than the circumference will decay (3). The motion of an annular thread of liquid on a wire was studied both theoretically and experimentally by Goren (4). Limiting his consideration to wires or tubes small enough that surface tension forces are much larger than gravitational forces, he found that the liquid film is unstable for sufficiently long wavelengths, and was able to calculate the most unstable wavelength. Hammon (5) and Gauglitz and Radke (6) extended the work of Goren, but their primary consideration was the coating on the inside of circular cylinders. Recently Mashayek and Ashgriz (7) used a height–flux method to model the full problem and identified growth rates and interfacial shapes as a function Reynolds number, disturbance amplitude, and cylinder radii.

The problem of a cylinder oriented with its axis parallel to gravity has also been studied, with the primary application being the growth of postapplication waves in the dip coating process. Lin and Liu considered the problem of an axisymmetric coating on a cylinder oriented with the axis parallel to gravity, and found a relationship between the Reynolds number and the stability of a given wavelength (8). Atherton and Homsy considered a similar problem, and derived an evolution equation based on the lubrication approximations (9). Kranz and Zollars started with the Orr–Sommerfeld equation and found a series solution valid for thin films and Reynolds numbers less than 0.5 (10). Shlang and Sivashinsky also derived an evolution equation and modeled certain aspects of chaos in the film (11). Solorio and Sen solved the complete problem numerically, and showed that the cylindrical falling film is unstable for all cylinder radii, Weber numbers, and finite Reynolds numbers (12).

The possibility that axial rotation of the cylinder may lead to centrifugal forces that counterbalance the draining force of gravity has been considered by several researchers. Moffatt derived an expression for the maximum liquid entrainment, and also investigated the onset of instabilities both theoretically and experimentally (13). Preziosi and Joseph confirmed Moffatt's results for thin films and presented further

[1] To whom correspondence should be addressed.

0021-9797/97 $25.00

experimental and theoretical verification (14). Hansen and Kelmanson used an iterative, integral equation formulation applied to the Stokes equations to consider coatings of arbitrary thickness (15). Stability criteria have been investigated by Dávalos-Orozco and Ruiz-Chavarría for small Reynolds numbers and wavenumbers (16).

The lubrication form of the unsteady two-dimensional evolution equation for simple liquids coating arbitrarily curved substrates was derived by Schwartz and Weidner (17). Results were presented for coatings in corner regions defined by a combination of flat and circular substrate segments. This was extended to include multicomponent, evaporating liquids by Weidner *et al.* (18).

Several researchers have considered the shape of steady-state pendant and sessile drops. Bashforth and Adams used hand-calculated tables to predict the shape of liquid drops on horizontal substrates as a function of surface tension and drop size (19). Hartland and Hartley used a fourth-order Runge–Kutta method to refine these calculations (20), and O'Brien used the method of matched asymptotic expansions to obtain the same profiles (21). Lawal and Brown considered the shape and stability of a pendant drop suspended from the end of an inclined circular tube (22). Using a finite-element method, they calculated the maximum drop volume as a function of tube radius and inclination angle.

In this study, we consider the motion of a simple liquid on a right circular cylinder oriented with the axial direction perpendicular to gravity. We derive the lubrication form of the three-dimensional, unsteady, coating evolution of a thin liquid film on a horizontal cylinder and simulate the formation of discrete drops on cylinders of various radii. We also consider the shape and volume of large-amplitude pendant drops. In Section II we derive the full equations of motion and boundary conditions for the free surface flow of a Newtonian liquid on a cylinder when the Reynolds number is small. Under the assumption that the slope of the free surface relative to the substrate is small, we perform a scaling analysis to extract a simpler set of equations which retain the essential nonlinear physics of the problem. Unlike standard implementations of lubrication theory, which use a small slope approximation to the radius of curvature, we retain the exact expression for the curvature, allowing a consistent evaluation of surface energy, as well as permitting us to predict the steady-state shape of large-amplitude pendant drops. In Section III we discuss the discretization and numerical solution to these equations. A modified alternating-direction implicit (ADI) method is presented and verification of the numerical implementation is demonstrated by comparing the numerical results with analytical results for various subproblems. Simulations are presented over a wide range of cylinder radii in Section IV, and show many interesting features of drop formation. Integral measures of the evolving patterns, such as the total energy, indicate that several growth regimes occur sequentially, with drainage of liquid from the top to the bottom of the cylinder preceding the formation of axial drops. Periods of drop formation and coalescence are shown to correspond with increases in the rate of viscous energy dissipation, and qualitative criteria for the extent to which drop shapes have evolved toward their equilibrium shapes are considered. In addition, we also consider the steady shape drop profile for large pendant drops on cylinders of various radii and calculate the maximum drop volume these cylinders may support. Conclusions are drawn in Section V. Applications of this work include coating and condensation on tubes, wires, and fibers and the condensation on larger cylindrical objects, such as pipes and ducts, in microgravity environments.

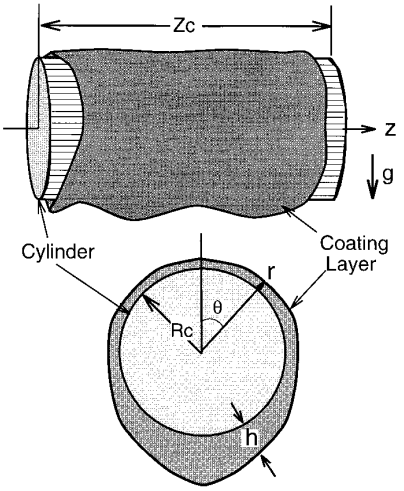

FIG. 1. Nomenclature and coordinate system.

II. MATHEMATICAL MODEL

A. Governing Equations

Consider a thin liquid film coating a solid right circular cylinder, oriented with its axis perpendicular to gravity, as shown in Fig. 1. Employing cylindrical coordinates (r, θ, z), the solid cylinder has a radius $r = R_c$, length $z = Z_c$, with θ representing a polar direction. The liquid is confined to a region $R_c \leqslant r \leqslant h$, where h, the thickness of the coating layer, is taken as a function of θ, z, and time t: $h = h(\theta, z, t)$.

With velocities in directions (r, θ, z) given by (v, u, w), respectively, and subscripts indicating partial differentiation, the continuity equation for an incompressible fluid in cylindrical coordinates takes the form

$$\frac{[rv]_r}{r} + \frac{u_\theta}{r} + w_z = 0. \qquad [1]$$

For small Reynolds numbers, the momentum equations in cylindrical coordinates, the Stokes equations, are given by

$$p_r = \mu\left[\frac{\partial}{\partial r}\left(\frac{1}{r}\frac{\partial}{\partial r}(rv)\right) + \frac{v_{\theta\theta}}{r^2} + v_{zz} - \frac{2u_\theta}{r^2}\right] - \rho g \cos\theta \quad [2]$$

$$\frac{p_\theta}{r} = \mu\left[\frac{\partial}{\partial r}\left(\frac{1}{r}\frac{\partial}{\partial r}(ru)\right) + \frac{u_{\theta\theta}}{r^2} + u_{zz} + \frac{2v_\theta}{r^2}\right] + \rho g \sin\theta \quad [3]$$

$$p_z = \mu\left[\frac{1}{r}\frac{\partial}{\partial r}(rw_r) + \frac{w_{\theta\theta}}{r^2} + w_{zz}\right]. \quad [4]$$

Here p is the pressure, ρ is the density and μ the viscosity of the liquid, and g the acceleration of gravity. At the surface of the solid cylinder, $r = R_c$, the no-slip boundary conditions are imposed:

$$v = u = w = 0. \quad [5]$$

The free surface is defined by the function F

$$F(r, \theta, z, t) = R_c + h(\theta, z, t) - r = 0, \quad [6]$$

and its unit normal vector $\hat{n}$ is given by

$$\hat{n} = \frac{\nabla F}{|\nabla F|} = \frac{-e^{(r)} + \left(\frac{h_\theta}{r}\right)e^{(\theta)} + h_z e^{(z)}}{\sqrt{1 + \left(\frac{h_\theta}{r}\right)^2 + (h_z)^2}}$$

at $r = R_c + h$. The material derivative of F must vanish, yielding the kinematic condition on the free surface $r = R_c + h$:

$$\frac{DF}{Dt} = 0 = h_t - v + u\left(\frac{h_\theta}{r}\right) + wh_z. \quad [7]$$

The mean curvature of the free surface for this geometry can be written

$$\kappa = -\nabla\cdot\hat{n} = \left\{\left(\frac{1}{r}\right)\left[1 + 2\left(\frac{h_\theta}{r}\right)^2 + h_z^2\right] - \left(\frac{h_{\theta\theta}}{r^2}\right)[1 + h_z^2] - h_{zz}\left[1 + \left(\frac{h_\theta}{r}\right)^2\right] + \frac{2h_\theta h_z h_{z\theta}}{r^2}\right\} \Big/ \sqrt{1 + \left(\frac{h_\theta}{r}\right)^2 + (h_z)^2}^{\,3} \quad [8]$$

at $r = R_c + h$. Neglecting the shear of the gas phase on the interface, and further assuming that the atmosphere is at zero pressure, a stress balance at the free surface, in tensor notation, is given by

$$[\tau_{ij} + p\delta_{ij}]\hat{n}_j = \sigma\kappa\hat{n}_i. \quad [9]$$

Here τ_{ij} is the stress tensor in the liquid at the interface and σ is the surface tension of the liquid. The three equations found by summing [9] over j for $i = r$, θ, and z, respectively, are

$$-p - \mu\left[r\frac{\partial}{\partial r}\left(\frac{u}{r}\right) + \frac{v_\theta}{r}\right]\frac{h_\theta}{r} + 2\mu v_r - \mu[w_r + v_z]h_z + \sigma\kappa = 0, \quad [10a]$$

$$-\mu\left[2\left(\frac{u_\theta}{r} + \frac{v}{r}\right)\right]\left(\frac{h_\theta}{r}\right) + \mu\left[r\frac{\partial}{\partial r}\left(\frac{u}{r}\right) + \frac{v_\theta}{r}\right] - \mu\left[u_z + \frac{w_\theta}{r}\right]h_z + p\frac{h_\theta}{r} - \sigma\kappa\frac{h_\theta}{r} = 0, \quad [10b]$$

$$-\mu\left[u_z + \frac{w_\theta}{r}\right]\frac{h_\theta}{r} + \mu[w_r + v_z] - \mu[2w_z]h_z + ph_z - \sigma\kappa h_z = 0, \quad [10c]$$

where all three equations are evaluated at $r = R_c + h$. Eliminating the pressure p and curvature κ from Eqs. [10b] and [10c] yields two equations expressing the condition of zero tangential stress at the interface,

$$-\left[2\left(\frac{u_\theta}{r} + \frac{v}{r}\right)\right]\frac{h_\theta}{r}h_z + \left[r\frac{\partial}{\partial r}\left(\frac{u}{r}\right) + \frac{v_\theta}{r}\right]h_z - \left[u_z + \frac{w_\theta}{r}\right]h_z^2 + \left[u_z + \frac{w_\theta}{r}\right]\left(\frac{h_\theta}{r}\right)^2 - [w_r + v_z]\frac{h_\theta}{r} + [2w_z]h_z\frac{h_\theta}{r} = 0, \quad [11a]$$

$$-\left(\frac{h_\theta}{r}\right)^3\left[r\frac{\partial}{\partial r}\left(\frac{u}{r}\right) + \frac{v_\theta}{r}\right] + \left(\frac{h_\theta}{r}\right)^2\left[-2\frac{u_\theta}{r} - 2\frac{v}{r} + 2v_r\right] - \frac{h_\theta}{r}\left[r\frac{\partial}{\partial r}\left(\frac{u}{r}\right) + \frac{v_\theta}{r}\right] - \frac{h_\theta}{r}h_z[2u_z + 2w_\theta] - \left(\frac{h_\theta}{r}\right)^2 h_z[w_r + v_z] - \frac{h_\theta}{r}(h_z)^2\left[r\frac{\partial}{\partial r}\left(\frac{u}{r}\right) - \frac{v_\theta}{r}\right] + (h_z)^3[-w_r - v_z] + (h_z)^2[2v_r - 2w_z] + h_z[w_r + v_z] = 0, \quad [11b]$$

with both equations evaluated at $r = R_c + h$.

The three momentum equations plus the continuity equation give four equations for the three unknown velocities, $v(r, \theta, z, t)$, $u(r, \theta, z, t)$, and $w(r, \theta, z, t)$, and the pressure $p(r, \theta, z, t)$. These four equations; the boundary conditions at the interface, provided by Eqs. [10a], [11a], and [11b]; the kinematic condition at the interface given by Eq. [7]; the boundary conditions at the substrate $r = R_c$, provided by Eqs. [5]; and the initial conditions constitute a complete statement of the problem. Unfortunately this set of equations is highly nonlinear, and complete numerical solutions tend to be difficult to implement and computationally intensive. In what follows, we obtain a simpler set of equations, which nonetheless incorporate the essential nonlinear physics of the problem, by exploiting the long-thin geometry of the liquid film. Specifically, we scale lengths in the θ and z directions by an order α smaller than lengths in the r direction, and determine the leading order equations using a systematic expansion of the velocity components in powers of α.

B. Scaling

Denoting scaled dimensionless variables by bars, we make the following transformations:

$$\bar{r} = \frac{r}{R_c}, \quad \bar{\theta} = \frac{\alpha R_c \theta}{h_0}, \quad \bar{z} = \frac{\alpha z}{h_0}, \quad \bar{t} = \frac{\alpha u_0 t}{h_0} \qquad [12]$$

$$\bar{v} = \frac{v}{\alpha u_0}, \ \bar{u} = \frac{u}{u_0}, \ \bar{w} = \frac{w}{u_0}, \ \bar{h} = \frac{h}{h_0}, \ \bar{\kappa} = R_c \kappa, \qquad [13]$$

where h_0 is a characteristic coating thickness and u_0 is a characteristic velocity. We begin by eliminating the pressure from the r, θ, and z momentum equations:

$$(p_\theta)_r - (p_r)_\theta = 0 = \frac{\partial}{\partial \bar{r}}\left[\bar{r}\frac{\partial}{\partial \bar{r}}\left(\frac{1}{\bar{r}}\frac{\partial}{\partial \bar{r}}(\bar{r}\bar{u})\right)\right] + O(\alpha^2), \qquad [14a]$$

$$(p_z)_r - (p_r)_z = 0 = \frac{\partial}{\partial \bar{r}}\left[\frac{1}{\bar{r}}\frac{\partial}{\partial \bar{r}}(\bar{r}\bar{w}_{\bar{r}})\right] + O(\alpha^2). \qquad [14b]$$

The scaled form of the continuity equation takes the form

$$\frac{[\bar{r}\bar{v}]_{\bar{r}}}{\bar{r}} + \frac{\bar{u}_{\bar{\theta}}}{H\bar{r}} + \frac{\bar{w}_{\bar{z}}}{H} = 0, \qquad [15]$$

where $H = h_0/R_c$, while the no-slip boundary conditions transform to

$$\bar{v}(\bar{r} = 1, \bar{\theta}, \bar{z}, \bar{t}) = \bar{u}(\bar{r} = 1, \bar{\theta}, \bar{z}, \bar{t}) = \bar{w}(\bar{r} = 1, \bar{\theta}, \bar{z}, \bar{t}) = 0. \qquad [16]$$

The scaled kinematic condition is given by

$$\bar{h}_{\bar{t}} - \bar{v} + \frac{\bar{u}\bar{h}_{\bar{\theta}}}{\bar{r}} + \bar{w}\bar{h}_{\bar{z}} = 0 \qquad [17]$$

at $\bar{r} = 1 + H\bar{h}$. The boundary conditions [11] transform to

$$\left(\frac{\bar{h}_{\bar{\theta}}}{\bar{r}}\right)\bar{r}\frac{\partial}{\partial \bar{r}}\left(\frac{\bar{u}}{\bar{r}}\right) + \bar{h}_{\bar{z}}\bar{w}_{\bar{r}} + O(\alpha^2) = 0, \qquad [18a]$$

$$\bar{h}_{\bar{z}}\bar{r}\frac{\partial}{\partial \bar{r}}\left(\frac{\bar{u}}{\bar{r}}\right) - \left(\frac{\bar{h}_{\bar{\theta}}}{\bar{r}}\right)\bar{w}_{\bar{r}} + O(\alpha^2) = 0, \qquad [18b]$$

with both equations evaluated at $\bar{r} = 1 + H\bar{h}$.

We do not transform the equation for the pressure discontinuity across the interface [10a] directly, but first eliminate the pressure from this equation using the momentum equations and identities for partial differentiation of implicit functions. From [10a] we know the pressure in the liquid at the free surface, $p(r = R_c + h, \theta, z, t)$. From the momentum equations, we know p_r, p_θ, and p_z everywhere in the liquid. The directional derivatives of p in the θ and z directions, respectively, along $r = R_c + h(\theta, z, t)$, are given by

$$[p_\theta + p_r h_\theta]|_{r=R_c+h} = \frac{\partial}{\partial \theta}p(r = R_c + h, \theta, z, t), \qquad [19]$$

$$[p_z + p_r h_z]|_{r=R_c+h} = \frac{\partial}{\partial z}p(r = R_c + h, \theta, z, t). \qquad [20]$$

The resultant scaled equations, evaluated at $r = R_c + h$, are

$$\frac{\partial}{\partial \bar{r}}\left(\frac{1}{\bar{r}}\frac{\partial}{\partial \bar{r}}(\bar{r}\bar{u})\right) = -\lambda \sin\theta + \alpha\left[\frac{\Lambda}{H}\frac{\bar{\kappa}_{\bar{\theta}}}{\bar{r}} + \frac{\lambda \bar{h}_{\bar{\theta}}\cos\theta}{\bar{r}}\right] + O(\alpha^2), \qquad [21a]$$

$$\frac{1}{\bar{r}}\frac{\partial}{\partial \bar{r}}(\bar{r}\bar{w}_{\bar{r}}) = \alpha\left[\frac{\Lambda}{H}\bar{\kappa}_{\bar{z}} + \bar{h}_{\bar{z}}\lambda\cos\theta\right] + O(\alpha^2), \qquad [21b]$$

where $\lambda = \rho g R_c^2/\mu u_0$ and $\Lambda = \sigma/\mu u_0$. Note that we have assumed that all κ terms are $O(1)$, not $O(\alpha^2)$ as suggested by Eq. [8]. We are, in effect, assuming that Λ is $O(1/\alpha^2)$ to bring the effects of surface tension into the $O(\alpha)$ problem. Benney (23), Atherton and Homsy (9), and others have employed a similar specific ''promotion'' for related thin-film problems.

We now represent the scaled velocities in regular perturbation expansions in powers of α,

$$\bar{v} = \bar{v}^{(0)} + \alpha\bar{v}^{(1)} + \cdots\alpha^n\bar{v}^{(n)},$$
$$\bar{u} = \bar{u}^{(0)} + \alpha\bar{u}^{(1)} + \cdots\alpha^n\bar{u}^{(n)},$$
$$\bar{w} = \bar{w}^{(0)} + \alpha\bar{w}^{(1)} + \cdots\alpha^n\bar{w}^{(n)}, \quad [22]$$

and solve for $\bar{v}^{(0)}$, $\bar{u}^{(0)}$, $\bar{w}^{(0)}$ and $\bar{v}^{(1)}$, $\bar{u}^{(1)}$, $\bar{w}^{(1)}$ using Eqs. [15]–[21]. The governing equations and boundary conditions for the zero-order problem are as follows:

$$\frac{(\bar{r}\bar{v}^{(0)})_{\bar{r}}}{\bar{r}} + \frac{\bar{u}^{(0)}_{\bar{\theta}}}{H\bar{r}} + \frac{\bar{w}^{(0)}_{\bar{z}}}{H} = 0, \quad [23]$$

$$\frac{\partial}{\partial\bar{r}}\left[\bar{r}\frac{\partial}{\partial\bar{r}}\left(\frac{1}{\bar{r}}\frac{\partial}{\partial\bar{r}}(\bar{r}\bar{u}^{(0)})\right)\right] = 0, \quad [24a]$$

$$\frac{\partial}{\partial\bar{r}}\left[\frac{1}{\bar{r}}\frac{\partial}{\partial\bar{r}}(\bar{r}\bar{w}^{(0)}_{\bar{r}})\right] = 0, \quad [24b]$$

$$\bar{v}^{(0)}(\bar{r} = 1, \theta, z, t) = \bar{u}^{(0)}(\bar{r} = 1, \theta, z, t) = \bar{w}^{(0)}(\bar{r} = 1, \theta, z, t) = 0. \quad [25]$$

Evaluated at $\bar{r} = 1 + H\bar{h}$,

$$\left(\frac{\bar{h}_{\bar{\theta}}}{\bar{r}}\right)\bar{r}\frac{\partial}{\partial\bar{r}}\left(\frac{\bar{u}^{(0)}}{\bar{r}}\right) + \bar{h}_{\bar{z}}\bar{w}^{(0)}_{\bar{r}} = 0, \quad [26a]$$

$$\bar{h}_{\bar{z}}\bar{r}\frac{\partial}{\partial\bar{r}}\left(\frac{\bar{u}^{(0)}}{\bar{r}}\right) - \left(\frac{H\bar{h}_{\bar{\theta}}}{\bar{r}}\right)\bar{w}^{(0)}_{\bar{r}} = 0, \quad [26b]$$

$$\frac{\partial}{\partial\bar{r}}\left(\frac{1}{\bar{r}}\frac{\partial}{\partial\bar{r}}(\bar{r}\bar{u}^{(0)})\right) = -\lambda\sin\theta, \quad [27a]$$

$$\frac{1}{\bar{r}}\frac{\partial}{\partial\bar{r}}(\bar{r}\bar{w}^{(0)}_{\bar{r}}) = 0. \quad [27b]$$

Integrating Eq. [24a] once yields

$$\bar{r}\frac{\partial}{\partial\bar{r}}\left(\frac{1}{\bar{r}}\frac{\partial}{\partial\bar{r}}(\bar{r}\bar{u}^{(0)})\right) = A_0(\theta, z, t), \quad [28]$$

where the function A_0 must be given by

$$A_0(\theta, z, t) = -\lambda[1 + Hh(\theta, z, t)]\sin\theta$$

from boundary condition [27a]. Noting that Eqs. [26a] and [26b] together require

$$\frac{\partial}{\partial\bar{r}}\left(\frac{\bar{u}^{(0)}}{\bar{r}}\right) = \bar{w}^{(0)}_{\bar{r}} = 0 \quad [29]$$

and using boundary conditions [25], two subsequent integrations yield an equation for the zero order u velocity

$$\bar{u}^{(0)} = -\lambda\frac{(1 + H\bar{h})\sin\theta}{2} \times\left[\bar{r}\ln\bar{r} - \frac{(1 + H\bar{h})^2}{2}\left[\bar{r} - \frac{1}{\bar{r}}\right]\right]. \quad [30]$$

Proceeding similarly with [24], we find

$$\bar{w}^{(0)} = 0. \quad [31]$$

The zero-order v velocity is found by integrating the continuity equation with the boundary conditions given by [25]:

$$\bar{v}^{(0)} = \frac{\lambda}{8}[(1 + H\bar{h})\cos\theta + \bar{h}_{\theta}\sin\theta] \times\left(\frac{2\bar{r}^2\ln\bar{r} - \bar{r}^2 + 1}{\bar{r}}\right) + \frac{\lambda}{8}[(1 + H\bar{h})^3\cos\theta + 3(1 + H\bar{h})^2\bar{h}_{\theta}\sin\theta]\left(\frac{2\ln\bar{r} - \bar{r}^2 + 1}{\bar{r}}\right). \quad [32]$$

The governing equations and boundary conditions for the order α problem are as follows:

$$\frac{[\bar{r}\bar{v}^{(1)}]_{\bar{r}}}{\bar{r}} + \frac{\bar{u}^{(1)}_{\bar{\theta}}}{H\bar{r}} + \frac{\bar{w}^{(1)}_{\bar{z}}}{H} = 0, \quad [33]$$

$$\frac{\partial}{\partial\bar{r}}\left[\bar{r}\frac{\partial}{\partial\bar{r}}\left(\frac{1}{\bar{r}}\frac{\partial}{\partial\bar{r}}(\bar{r}\bar{u}^{(1)})\right)\right] = 0, \quad [34a]$$

$$\frac{\partial}{\partial\bar{r}}\left[\frac{1}{\bar{r}}\frac{\partial}{\partial\bar{r}}(\bar{r}\bar{w}^{(1)}_{\bar{r}})\right] = 0, \quad [34b]$$

$$\bar{v}^{(1)}(\bar{r} = 1, \bar{\theta}, \bar{z}, \bar{t}) = \bar{u}^{(1)}(\bar{r} = 1, \bar{\theta}, \bar{z}, \bar{t}) = \bar{w}^{(1)}(\bar{r} = 1, \bar{\theta}, \bar{z}, \bar{t}) = 0. \quad [35]$$

Evaluated at $\bar{r} = 1 + H\bar{h}$,

$$\left(\frac{\bar{h}_{\bar{\theta}}}{\bar{r}}\right)\bar{r}\frac{\partial}{\partial\bar{r}}\left(\frac{\bar{u}^{(1)}}{\bar{r}}\right) + \bar{h}_{\bar{z}}\bar{w}^{(1)}_{\bar{r}} = 0, \quad [36a]$$

$$\bar{h}_{\bar{z}}\bar{r}\frac{\partial}{\partial\bar{r}}\left(\frac{\bar{u}^{(1)}}{\bar{r}}\right) - \left(\frac{\bar{h}_{\bar{\theta}}}{\bar{r}}\right)\bar{w}^{(1)}_{\bar{r}} = 0, \quad [36b]$$

$$\frac{\partial}{\partial \bar{r}}\left(\frac{1}{\bar{r}}\frac{\partial}{\partial \bar{r}}(\bar{r}\bar{u}^{(1)})\right) = \frac{1}{\bar{r}}\left[\frac{\Lambda}{H}\bar{\kappa}_{\bar{\theta}} + \lambda\bar{h}_{\bar{\theta}}\cos\theta\right], \quad [37a]$$

$$\frac{1}{\bar{r}}\frac{\partial}{\partial \bar{r}}(\bar{r}\bar{w}_{\bar{r}}^{(1)}) = \left[\frac{\Lambda}{H}\bar{\kappa}_{\bar{z}} + \lambda\bar{h}_{\bar{z}}\cos\theta\right]. \quad [37b]$$

Integrating Eq. [34a] and applying the appropriate boundary conditions yields the order α velocity in the θ direction:

$$\bar{u}^{(1)} = \frac{(\lambda\bar{h}_{\bar{\theta}}\cos\theta + (\Lambda/H)\bar{\kappa}_{\bar{\theta}})}{2} \times \left[\bar{r}\ln\bar{r} - \frac{(1+H\bar{h})^2}{2}\left[\bar{r} - \frac{1}{\bar{r}}\right]\right]. \quad [38]$$

Proceeding similarly with [34b], we find

$$\bar{w}^{(1)} = \frac{((\Lambda/H)\kappa_{\bar{z}} + \lambda\bar{h}_{\bar{z}}\cos\theta)}{4} \times [\bar{r}^2 - 2(1+H\bar{h})^2\ln\bar{r} - 1]. \quad [39]$$

The order α velocity in the r direction may be found by integrating the continuity equation with the boundary conditions given by [35], but limiting our consideration to the order α problem, it is possible to write the evolution equation in divergence form without solving explicitly for $\bar{v}^{(1)}$. Integrating the continuity equation between $\bar{r} = 1$ and $\bar{r} = 1 + H\bar{h}$, and using Leibniz's rule, the kinematic condition takes the form

$$\bar{h}_{\bar{t}} = \frac{-1}{(1+H\bar{h})}\left[\frac{\partial Q^{(\bar{\theta})}}{\partial\bar{\theta}} + \frac{\partial Q^{(\bar{z})}}{\partial\bar{z}}\right], \quad [40]$$

with the fluxes given by

$$Q^{(\bar{\theta})} = \int_1^{1+H\bar{h}}\bar{u}d\bar{r}, \quad Q^{(\bar{z})} = \int_1^{1+H\bar{h}}\bar{r}\bar{w}d\bar{r}. \quad [41]$$

To order α, the divergence form for the evolution equation is given by

$$\bar{h}_{\bar{t}} = -\frac{1}{(1+H\bar{h})}\left[\frac{-\lambda(1+H\bar{h})\sin\theta}{2} \times \left[(1+H\bar{h})^2\ln(1+H\bar{h}) - H\bar{h}\left(1 + \frac{3H\bar{h}}{2} + (H\bar{h})^2 + \frac{(H\bar{h})^3}{4}\right)\right]\right]_{\bar{\theta}}$$

$$- \alpha\left\{\frac{1}{(1+H\bar{h})}\left[\frac{(\Lambda/H)\bar{\kappa}_{\bar{\theta}} + \lambda\bar{h}_{\bar{\theta}}\cos\theta}{2} \times \left[(1+H\bar{h})^2\ln(1+H\bar{h}) - H\bar{h}\left(1 + \frac{3(H\bar{h})}{2} + (H\bar{h})^2 + \frac{(H\bar{h})^3}{4}\right)\right]\right]_{\bar{\theta}}\right.$$

$$\left. + \frac{1}{(1+H\bar{h})}\left[\left(\frac{\Lambda\bar{\kappa}_{\bar{z}}}{H} + \lambda\bar{h}_{\bar{z}}\cos\theta\right)\left[-\ln(1+Hh)\left(\frac{1}{4} + H\bar{h} + \frac{3(H\bar{h})^2}{2} + (H\bar{h})^3 + \frac{(H\bar{h})^4}{4}\right) + \frac{H\bar{h}}{4} + \frac{7(H\bar{h})^2}{8} + \frac{3(H\bar{h})^3}{4}\right]\right]_{\bar{z}}\right\}. \quad [42]$$

Returning to physical variables, the evolution equation is

$$h_t = -\frac{1}{\mu(R_c+h)}\left\{\left[(\rho g(R_c+h)\sin\theta - \sigma\kappa_\theta - \rho g h_\theta\cos\theta)G_1(h)\right]_\theta + R_c^2\left[-(\sigma\kappa_z + \rho g h_z\cos\theta)G_2(h)\right]_z\right\}, \quad [43]$$

where the functions $G_1(h)$ and $G_2(h)$ are given by

$$G_1(h) = R_c^2\left[-\left(1+\frac{h}{R_c}\right)^2\ln\left(1+\frac{h}{R_c}\right) + \frac{h}{R_c} \times \left[1 + \frac{3}{2}\frac{h}{R_c} + \left(\frac{h}{R_c}\right)^2 + \frac{1}{4}\left(\frac{h}{R_c}\right)^3\right]\right],$$

$$G_2(h) = R_c^2\left[\ln\left(1+\frac{h}{R_c}\right)\left(\frac{1}{4} + \frac{h}{R_c} + \frac{3}{2}\left(\frac{h}{R_c}\right)^2 + \left(\frac{h}{R_c}\right)^3 + \frac{1}{4}\left(\frac{h}{R_c}\right)^4\right) - \frac{1}{4}\left(\frac{h}{R_c}\right) - \frac{7}{8}\left(\frac{h}{R_c}\right)^2 - \frac{3}{4}\left(\frac{h}{R_c}\right)^3\right].$$

Expanding the logarithmic terms in the two functions for small h/R_c yields

$$G_1(h) = G_2(h) = R_c^2\left[\frac{1}{3}\left(\frac{h}{R_c}\right)^3 + O\left(\frac{h}{R_c}\right)^4\right]. \quad [44]$$

C. Nondimensionalization

We now nondimensionalize the evolution equation using a different scaling. All lengths will be scaled with the capillary length, $l_c = \sqrt{\sigma/\rho g}$, and we define

$$\hat{r} = \frac{r}{l_c}, \quad \hat{z} = \frac{z}{l_c}, \quad \hat{R}_c = \frac{R_c}{l_c}, \quad \hat{h} = \frac{h}{l_c},$$

$$\hat{\kappa} = \kappa l_c, \quad \hat{t} = t\,\frac{\sqrt{\sigma\rho g}}{3\mu}. \quad [45]$$

Henceforth dropping the hats, the nondimensional form of [43] is

$$h_t = \frac{-1}{(R_c + h)}\left\{\left[\left((R_c + h)\sin\theta - \kappa_\theta - h_\theta\cos\theta\right)\frac{h^3}{R_c}\right]_\theta + \left[(-\kappa_z - h_z\cos\theta)R_c h^3\right]_z\right\}. \quad [46]$$

III. NUMERICAL ASPECTS

A. Method

To solve Eq. [46] numerically, we discretize the θ, z, t domain and use a finite-difference method to represent the partial derivatives. The highest derivatives in Eq. [46] come from the κ terms, and are of fourth order. Hence for a totally explicit scheme to be stable it would be necessary to have

$$\Delta t < O(\Delta^4) \quad [47]$$

when $\Delta = \Delta z = R_c\Delta\theta$. This is a severe requirement, making multidimensional unsteady calculations with good spatial resolution impractical. Stability can be greatly enhanced by treating the high derivatives of κ implicitly. In addition, nonlinear prefactors, such as the h^3 terms in Eq. [46], will be treated explicitly in our numerical scheme. All lower derivatives of κ may also be treated explicitly.

The discretized quantities are $\theta_i = i\Delta\theta$, $z_j = j\Delta z$, $t = k\Delta t$, and $h = h^k_{i,j}$, where the superscript k is the time level. We solve the discretized evolution equation using an ADI method similar to that developed by Conte and Dames for the biharmonic equation (24). We first sweep through the domain, treating all higher θ derivatives of κ implicitly and all z derivatives and lower θ derivatives explicitly. In the next time step, which is a corrector step, higher z derivatives, which were treated explicitly in the predictor step, are treated implicitly.

First we introduce the new quantities

$$\Delta h^{k+1/2} = h^{k+1/2} - h^k, \quad \Delta h^{k+1} = h^{k+1} - h^{k+1/2}, \quad [48]$$

where the $k + 1/2$ level is always the ''predicted'' time level. We first sweep the domain, treating higher θ derivatives implicitly and z derivatives explicitly, and solve for $\Delta h^{k+1/2}$

$$\frac{\Delta h^{k+1/2}_{i,j}(R_c + h^k_{i,j})}{\Delta t} = -\left\{[[\tilde{A}^k_{i,j} + \tilde{B}^{k+1/2}_{i,j}](h^k_{i+1/2,j})^3 - [\tilde{A}^k_{i-1,j} + \tilde{B}^{k+1/2}_{i-1,j}](h^k_{i-1/2,j})^3]\left(\frac{1}{R_c\Delta\theta}\right) + [[\tilde{C}^k_{i,j}](h^k_{i,j+1/2})^3 - [\tilde{C}^k_{i,j-1}](h^k_{i,j-1/2})^3]\left(\frac{R_c}{\Delta z}\right)\right\}. \quad [49]$$

With $\Delta h^{k+1/2}$ found, we determine $h^{k+1/2}$ using (48). We again sweep the domain, treating high z derivatives implicitly, and solve for $\Delta h^{k+1}_{i,j}$:

$$\frac{\Delta h^{k+1}_{i,j}(R_c + h^{k+1/2}_{i,j})}{\Delta t} = -\left\{[[\tilde{D}^{k+1}_{ij} + \tilde{E}^{k+1/2}_{i,j}](h^{k+1/2}_{i,j+1/2})^3 - [\tilde{D}^{k+1}_{i,j-1} + \tilde{E}^{k+1/2}](h^{k+1/2}_{i,j-1/2})^3 + [-\tilde{E}^k_{i,j}] \times (h^k_{i,j+1/2})^3 - [-\tilde{E}^k_{i,j-1}](h^k_{i,j-1/2})^3]\left(\frac{R_c}{\Delta z}\right)\right\}. \quad [50]$$

Note that nonlinear $(h^k_{i\pm1/2,j})^3$ and $(h^{k+1/2}_{i\pm1/2,j})^3$ terms are interpolated from known values of h^k and $h^{k+1/2}$, respectively.

The functions $\tilde{A}$, $\tilde{B}$, $\tilde{C}$, $\tilde{D}$, and $\tilde{E}$ are defined as follows:

1. $\tilde{A}$ are explicit terms from the discretized form of the expression $[(R_c + h)\sin\theta - \kappa_\theta - h_\theta\cos\theta]$ in the evolution equation using central differences for all θ and z derivatives.
2. $\tilde{B}$ are terms from the θ derivative of the second term in Eq. [8], with all higher θ derivatives treated implicitly.
3. $\tilde{C}$ are explicit terms from the discretized form of the expression $[-\kappa_z - h_z\cos\theta]$ in the evolution equation and always evaluated at the k time level.
4. $\tilde{D}$ are terms from the z derivative of the fourth term in Eq. [8], with all higher z derivatives treated implicitly.
5. $\tilde{E}$ are terms from the z derivative of the fourth term in Eq. [8], treated explicitly, at the k time level for $\tilde{E}^k$ and the known ''predicted'' time level for $\tilde{E}^{k+1/2}$.

Using this algorithm, sets of pentadiagonal systems of equations must be solved twice at each time step to determine $\Delta h^{k+1/2}_{i,j}$ and $\Delta h^{k+1}_{i,j}$.

The volume of the liquid region is given by

$$V = \int_0^\pi \int_0^{z_{\max}} \frac{h}{2}(2R_c + h)\,d\theta dz, \quad [51]$$

or in discretized form,

$$V = \sum_j \sum_i \left(\frac{[h_{i,j}]^2}{2} + R_c h_{i,j} \right) \Delta\theta \Delta z + O(\Delta^4). \quad [52]$$

Mass conservation requires

$$\frac{\partial V}{\partial t} = \int_0^{\pi} \int_0^{z_{\max}} \frac{\partial h}{\partial t} [h + R_c] d\theta dz = 0. \quad [53]$$

When zero flux boundary conditions are prescribed at all four boundaries of the computational domain the above algorithm enforces

$$\sum_j \sum_i \Delta h_{i,j}^{k+1/2} [R_c + h_{i,j}^k] = 0$$

$$\text{and} \quad \sum_j \sum_i \Delta h_{i,j}^{k+1} [R_c + h_{i,j}^{k+1/2}] = 0, \quad [54]$$

which is simply the discrete form of Eq. [53], and mass is conserved to order $O(\Delta^4)$.

B. Verification

There exist analytic solutions for the coating distribution on a cylinder for two limiting cases: (i) The steady-state coating profile of a finite cylinder in the absence of gravity; (ii) the steady-state coating profile of cylinder with no axial variation in the coating layer. We use the results of our time-dependent algorithm at large time, when steady state has essentially been reached, and compare our numerical results with the two cases listed above.

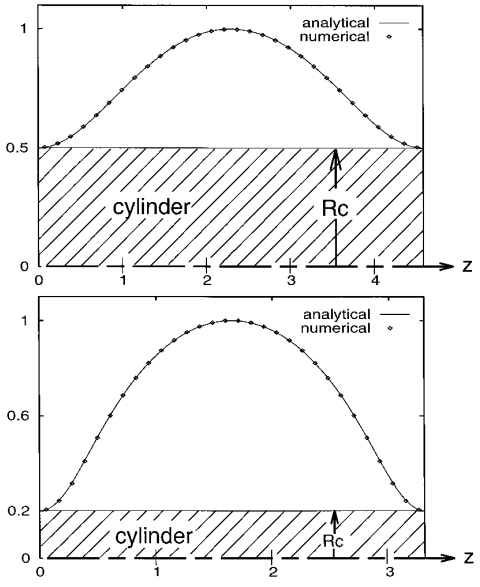

FIG. 2. Comparison of axisymmetric coating profiles produced using the numerical algorithm and an analytical solution found using elliptic integrals, for two different values of R_c.

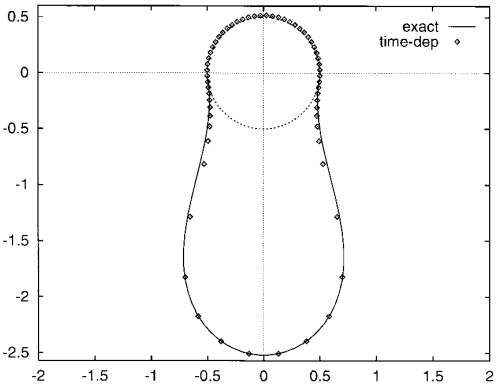

FIG. 3. Validation for a two-dimensional, steady-state pendant liquid drop of maximum area.

For the first case, the solution for a given R_c can be expressed in closed form using elliptic integrals (25). It is also a special case of the axisymmetric solution for spinning cylinders given by Joseph and Preziosi (26). In our simulation, we begin with a cosine wave of length $Z_{\max}$ and initial amplitude chosen to enclose the same fluid volume as determined from the analytic solution. We then run the simulation until h_t is negligibly small everywhere and steady state has essentially been reached. The results are shown in Fig. 2 for two different R_c values, and show close agreement between the numerical predictions and the analytical results.

For the second case, a solution can be obtained by integrating the ordinary differential equation expressing the condition of zero flux,

$$[(R_c + h)\sin\theta - \kappa_\theta - h_\theta \cos\theta] = 0,$$

using the boundary conditions

$$h_\theta = 0, \quad h = 0 \qquad \text{at } r = R_c,$$
$$h_\theta = 0, \quad h = h_{\max} \quad \text{at } \theta = \pi,$$

with κ given by Eq. [8] with $h_z = h_{zz} = 0$. The value of $h_{\max}$ was determined using the time-dependent program with no z variation, and corresponds to the drop of maximum cross-sectional area that a cylinder can support. The time-dependent steady-state solution shown in Fig. 3 is close to the exact solution, and the discrepancies in the region of the cylinder are due to the coarse grid and the fact that the contact angle for the numerical solution is not exactly zero.

In addition, convergence of the solution under spatial and temporal refinement was verified for a variety of other cases.

IV. RESULTS

In this section we consider two distinct problems. First we use the time-dependent algorithm developed in Section

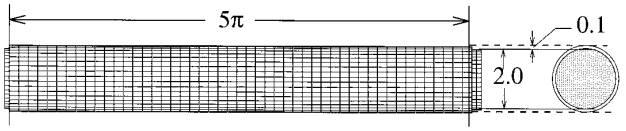

FIG. 4. Two views of the initial coating profile for the $R_c = 1$ case. The cylinder has a length of 5π, and the initial coating layer is given by $h(z, \theta) = 0.1 + \epsilon(z, \theta)$.

III to simulate the coating behavior of liquids on cylinders of various radii. For these cases, we restrict our considerations to thin films where the slope of the air–liquid interface is everywhere small relative to the substrate, and model the entire evolution of the film. For these cases the lubrication approximation is always valid, and we expect to capture nonlinear effects correctly. Second, we allow much larger liquid volumes and consider only the final state, where surface tension exactly balances gravity and viscous forces are negligible. For both of these cases, we consider cylinders of radii from 0.125 to 2. For terrestrial gravity, where the capillary length is $l_c \approx 0.25$ cm, these radii correspond to cylinders with diameters from 0.0625 to 1.0 cm. But for microgravity environments, the simulations can correspond to cylinders with much larger diameters.

A. Drop Evolution

Figure 4 shows the initial state of the canonical problem considered in this section. A right circular cylinder of radius 1.0 and length 5π is coated with a uniform film of thickness $h_0 = 0.1$ at $t = 0$. (All lengths are in units of the capillary length l_c.) Low-level white noise (maximum amplitude 10^{-6} l_c) is applied to the free surface, and we model the coating evolution as discrete drops form on the cylinder. In Figs. 5–8 we plot the coating thickness at the cylinder bottom for four distinct phases of drop evolution. In phase 1, illustrated by Fig. 5, the liquid drains under gravity and there is very little variation in the axial direction. Longitudinal waves that

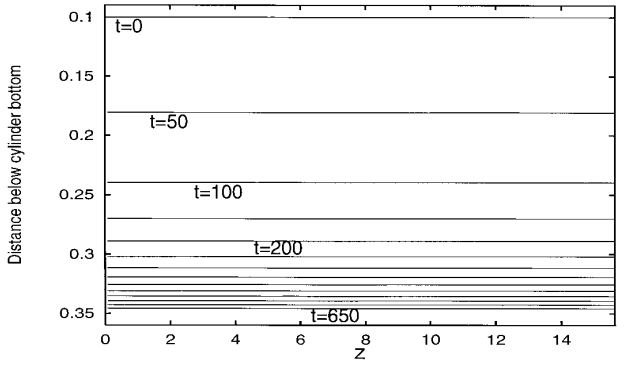

FIG. 5. Coating profiles during phase 1: Drainage of liquid from the top and sides of the cylinder toward the cylinder bottom. Here gravity-driven drainage damps the growth of any longitudinal waves. Coating profiles plotted as distance below the bottom of the cylinder versus axial distance along cylinder z from $t = 0.0$ to $t = 650.0$. Here $R_c = 1$.

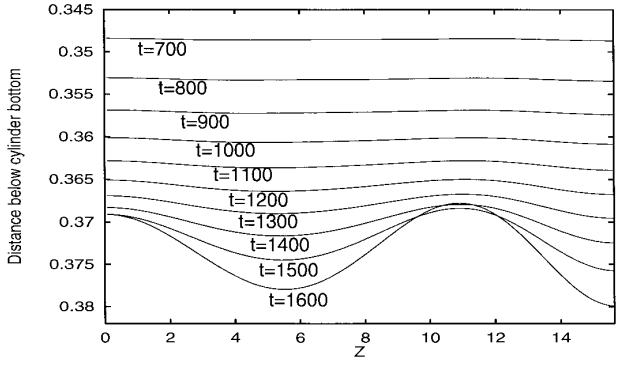

FIG. 6. Coating profiles during phase 2: The development of a small-amplitude longitudinal wave along the cylinder bottom. Here $R_c = 1$.

begin to form during this period are damped by the gravity-driven drainage from the top and sides of the cylinder toward the cylinder bottom. In phase 2, illustrated in Fig. 6, the drainage slows, and a low-amplitude longitudinal disturbance begins to grow. The wavelength of this disturbance is approximately 10.5. By comparison, a linear stability analysis predicts the most unstable wavelength for a two-dimensional disturbance on the underside of a flat substrate to be $2\pi\sqrt{2} \approx 8.88$. For an identical simulation but with a much larger Z_{max}, the initial low-amplitude wavelength is approximately 8.9, demonstrating that the wavelength for this simulation is influenced by the enforced zero-slope boundary conditions at the two ends of the cylinder. Phase 3, shown in Fig. 7, shows the transition from a linear to a nonlinear growth regime. For times between 1700 and approximately 2200, the growth rate of the disturbance increases. For times greater than $t = 2200$, the amplitude grows at a decreasing rate at the two crests, and higher harmonics appear in the two troughs as the wave first flattens, and then divides into two waves in this region. This nonlinear division produces a small-amplitude drop between two large-amplitude drops, sometimes referred to as a satellite drop (27). In phase 4, shown in Fig. 7, the evolution slows as the drop profile approaches its steady-state shape. During this phase, the sat-

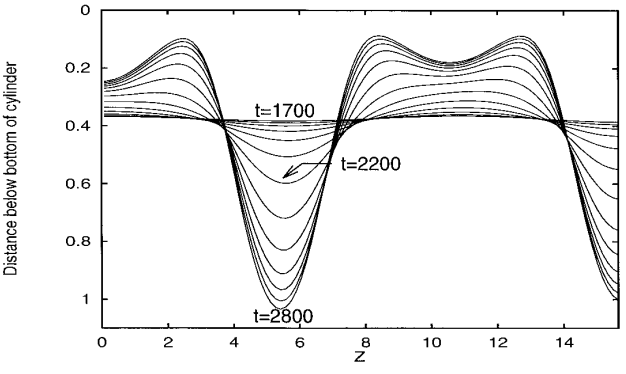

FIG. 7. Coating profiles during phase 3: Transition from linear to nonlinear regime with the formation of large-amplitude primary drops and smaller satellite drops. Here $R_c = 1$.

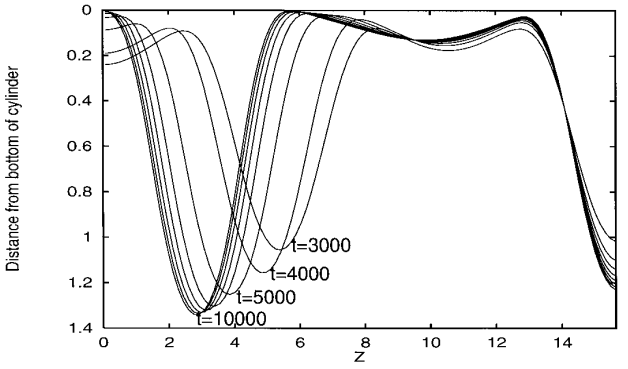

FIG. 8. Coating profiles during phase 4: Drop movement and coalescence, followed by the approach to a steady-state configuration. Here $R_c = 1$.

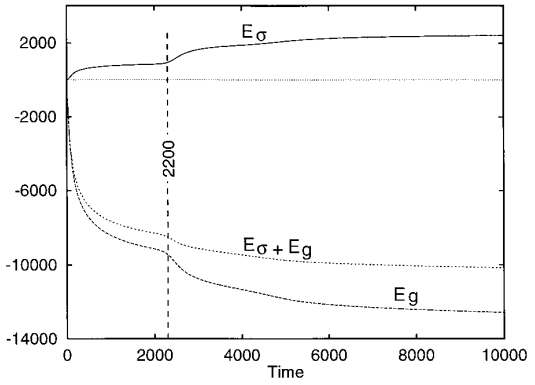

FIG. 9. Surface tension energy E_σ, gravitational potential energy E_g, and their sum plotted versus time for the $R_c = 1$ case. The inflection in the three curves near $t = 2200$ corresponds to the transition from the linear to nonlinear regime with the formation of large-amplitude primary drops and smaller satellite drops. The value of E_σ has been normalized to 0.0 at $t = 0.0$.

ellite and a main drop on the left coalesce to form a single drop, and the wavelength of the remaining satellite drop increases. This drop movement and coalescence are due, in part, to the enforced zero-slope, zero-flux boundary conditions at $z = 0$ and $z = 5\pi$. Thus, at both ends of the cylinder there must be a drop crest or trough, with a half-integral number of drops between these two boundary drops. At steady state the sum of the total volume of these drops must equal the initial volume of liquid.

The results presented in Figs. 5 through 8 are for one simulation with an initial random noise amplitude of 10^{-6} l_c. We are dealing with an inherently nonlinear problem, and the possibility of large changes in the final state due to small changes in the initial conditions must always be considered. For this problem, however, most of the qualitative features discussed in the preceding paragraph are fairly robust and are not greatly modified using different initial conditions. We have investigated the matter and found that while increasing the noise amplitude or starting with a low-amplitude longitudinal wave changes such features as the nonlinear time onset and the location and amplitude of the primary and satellite drops, it does not affect the number of primary drops that form on a cylinder of a given length. Numerical experiments indicate that the qualitative features of drop formation considered in this section are largely independent of the initial conditions.

It is informative to compare the various stages of drop growth with the total potential and dissipated energy of the system. The surface tension energy, proportional to the area of the free surface, is

$$E_\sigma = \iint [h_z^2(h + R_c)^2 + h_\theta^2 + (h + R_c)^2]^{1/2} d\theta dz, \quad [55]$$

while the gravitational potential energy is given by

$$E_g = \iint \cos\theta \left[\frac{(R_c + h)^3}{3} - \frac{R_c^3}{3} \right] d\theta dz, \quad [56]$$

where h and R_c are in units of l_c and the nondimensional energies E_σ and E_g are in units of $\sigma^2/\rho g$.

Figure 9 plots E_σ, E_g, and $E_\sigma + E_g$ for the four phases shown in Figs. 5–8, with E_σ and E_g normalized to 0 at $t = 0$. The surface tension energy, and therefore the area of the free surface, increases monotonically over the time range $0 \leqslant t \leqslant 10^5$. The gravitational potential energy monotonically decreases over the same interval, and both curves have an inflection point at approximately $t = 2200$, which, from Fig. 7, corresponds to the time of large drop formation on the cylinder. Energy is lost in this system through viscous heating, given by $\dot{E}_\mu$, and from conservation of energy we find

$$\dot{E}_\mu = -(\dot{E}_\sigma + \dot{E}_g). \quad [57]$$

The region of drop coalescence is not shown clearly in Fig. 9, but Fig. 10, which plots $\dot{E}_\mu$ versus time, clearly shows the time frame for drop movement and coalescence between t

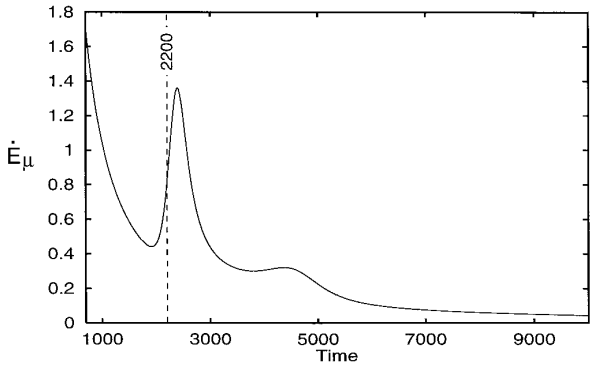

FIG. 10. Rate of energy dissipated in viscous heating, $\dot{E}_\mu = -(\dot{E}_\sigma + \dot{E}_g)$, plotted as a function of time for the $R_c = 1$ case. The transition from the linear to nonlinear regime occurs near $t = 2200$, while the small peak at $4000 \leqslant t \leqslant 5000$ corresponds to lateral drop movement and coalescence.

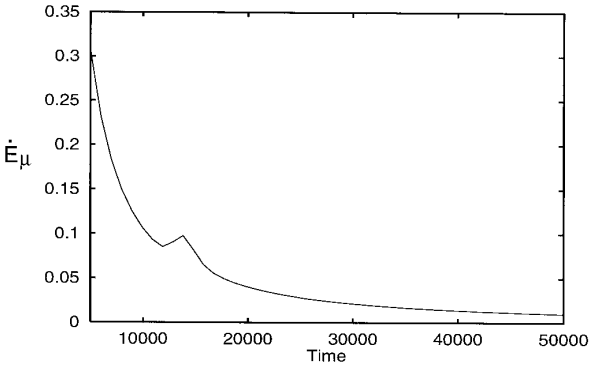

FIG. 11. $\dot{E}_\mu = -(\dot{E}_\sigma + \dot{E}_g)$ plotted as a function of time for the $R_c = 2$ case. The peak near $t = 14{,}000$ corresponds to the time of drop formation on the underside of the cylinder.

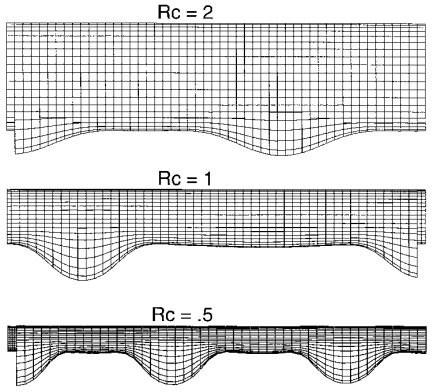

FIG. 13. Profile view of the coating distributions at large time for the three cases $R_c = 2$, $R_c = 1$, $R_c = 0.5$.

$= 4000$ and $t = 5000$, as well as the formation of large-amplitude drops starting near $t = 2200$.

Thus far we have considered only the $R_c = 1$ case, but plots of $\dot{E}_\mu$ versus time for the $R_c = 2$ and $R_c = 0.5$ cases show similar peaks at the time of drop formation, as shown in Figs. 11 and 12. For these cases there is only one peak at the time of drop formation, and drop coalescence does not occur, though there is a slow drainage from the satellite drops into the primary drops in both cases. Figure 13 shows the long-time, quasi-steady-state, three-dimensional profile of the cylinder and coating for cylinder radii of 2.0, 1.0, and 0.5. In all three cases the starting volume, noise amplitude, and cylinder length are the same.

For the three cylinder radii considered above, the surface area, and therefore the surface energy, increases monotonically with time, while the gravitational potential energy always decreases. But on length scales where the effects of surface tension forces are comparable to gravitational forces, we expect that the surface area may decrease, even if this requires an increase in the gravitational potential energy. Such a situation occurs for a cylinder radius of 0.125, corresponding to a Bond number of 0.015 based on cylinder radius, $\rho g R_c^2/\sigma = 0.015$. Figure 14 is a plot of the potential energies versus time for the $R_c = 0.125$ case. Here $h_0 = R_c/5$, $Z_{max} = 1.25\pi$, and the maximum noise amplitude is $10^{-6}\, l_c$. In contrast to previous results, the surface tension energy decreases with time and the gravitational potential energy, which initially decreases as the liquid drains, increases at the time of large drop formation. Figure 15 shows the drop formation on the underside of the cylinder for the same simulation plotted in Fig. 14. Qualitatively this graph is similar to that shown in Fig. 6 for the $R_c = 1.0$ case. After most of the liquid has drained from the top and sides of the cylinder, a low-amplitude longitudinal disturbance grows and primary and satellite drops form during the transition from the linear to nonlinear growth regime. But in this case, the gravitational potential energy *increases* during this drop formation phase. The reason for this is clear from Figs. 16–19 where we have ''unwrapped'' the cylinder to show a plot of h versus z and arc length $x = R_c\theta$, for four different times. As with the case of larger radii, the liquid first drains toward the bottom until only a thin layer remains at the top of the

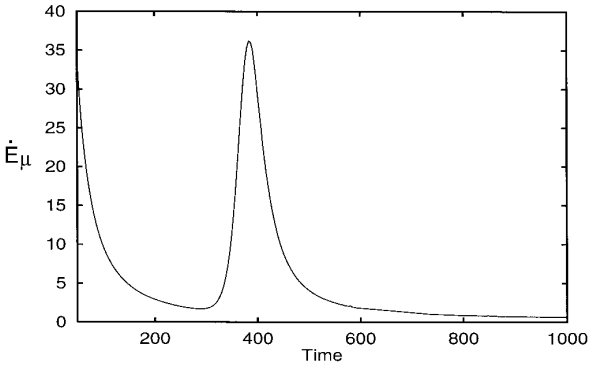

FIG. 12. Rate of energy dissipated in viscous heating, $\dot{E}_\mu = -(\dot{E}_\sigma + \dot{E}_g)$, plotted as a function of time for the $R_c = 0.5$ case. The peak near $t = 400$ corresponds to the time of drop formation on the underside of the cylinder.

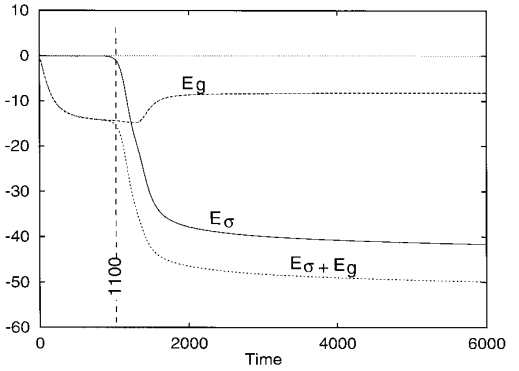

FIG. 14. Surface tension energy E_σ, gravitational potential energy E_g, and their sum plotted versus time for the $R_c = 0.125$ case. From $0 \leqslant t \leqslant 1000$, E_g decreases as the coating drains toward the bottom of the cylinder. At $t = 1100$, large-amplitude longitudinal waves begin to form, decreasing the surface area and therefore E_σ. At $t \approx 1600$, liquid is drawn upward against gravity and drops form on the top of the cylinder. The value of E_σ has been normalized to 0.0 at $t = 0.0$.

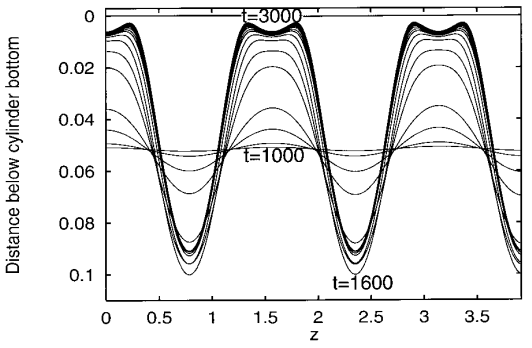

FIG. 15. Coating profiles plotted as distance below the bottom of the cylinder versus axial distance along cylinder z during the period of large-amplitude and satellite drop formation for the $R_c = 0.125$ case. For $t \leqslant 1000$, the coating drains under gravity and there is very little variation in the z direction. For $1100 \leqslant t \leqslant 1500$, large-amplitude longitudinal waves grow to form discrete drops on the cylinder bottom. At $t \approx 1600$, liquid is drawn toward the top of the cylinder, reducing the amplitude at the crests along the bottom. For larger times, satellite drops form and the coating evolution slows as the profile moves toward steady state.

cylinder. But when large-amplitude drops begin to form along the cylinder bottom, liquid is drawn back to the top of the cylinder. The large-amplitude drops are not confined to the underside of the cylinder, but wrap around the circumference of the cylinder and cover portions of the top of the cylinder. The surface tension energy decreases because the large-amplitude waves have a lower surface area than a uniform coating, but the gravitational potential energy increases during this period as liquid is pushed upward to the top surface of the cylinder. This result may be important in applications where it is desired to limit the thinning of coatings on small cylinders due to gravitational drainage, for it indicates that the coating distribution will be substantially more uniform for cylinders below a critical nondimensional radius R_c.

Figure 15 also shows that the wavelength of the initial disturbance is much less than that for the $R_c = 1$ case. For this value of R_c, surface tension is much more important than gravity, and the wavelength of the initial disturbance is close to the most unstable wavelength predicted by linear theory for a coating on a cylinder in the absence of gravity, $\lambda = 2\pi\sqrt{2}(R_c + h) \approx 1.55$.

The rate of viscous dissipation with time is also of interest for this case. As with the $R_c = 1$ case, the rate of dissipation increases dramatically during the formation of the high-amplitude drops, as shown in Fig. 20. There is also a secondary plateau at approximately $t = 1500$, which corresponds to the time of upward flux toward the top of the cylinder and the formation of satellite drops due to the appearance of higher harmonics in the drop troughs, as described for the $R_c = 1$ simulation.

For all the simulations presented, the coating liquid first drains toward the bottom of the cylinder and then forms a series of primary and satellite drops along the horizontal axis of the cylinder. These drops will reach a state of static equilibrium when the hydrostatic pressure difference exactly balances the pressure drop across the interface due to surface tension, i.e.,

$$\kappa + (R_c + h)\cos\theta = C, \qquad [58]$$

where C is a constant. This state will be reached only exactly at infinite time. Equation [58] is also satisfied when the sum of the two potential energies, E_σ and E_g, is at a minimum within the constraint of constant volume,

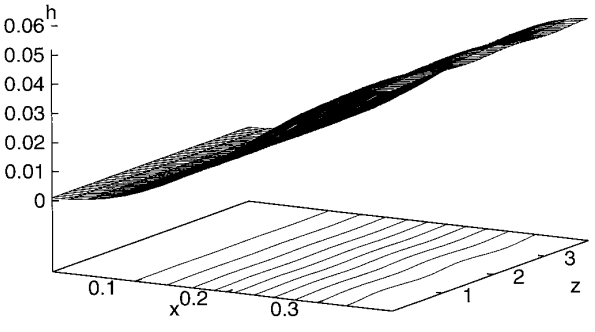

FIG. 16. Surface plot of h versus x and z, with contours, for the $R_c = 0.125$ case at $t = 900$. Here most of the liquid has drained from the top of the cylinder toward the bottom half of the cylinder.

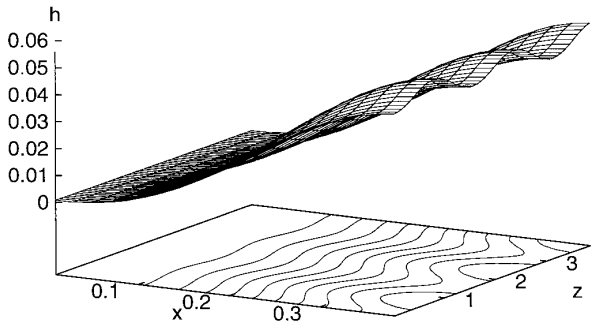

FIG. 17. Surface plot of h versus x and z, with contours, for the $R_c = 0.125$ case at $t = 1200$. Here small-amplitude waves begin to form near the cylinder bottom.

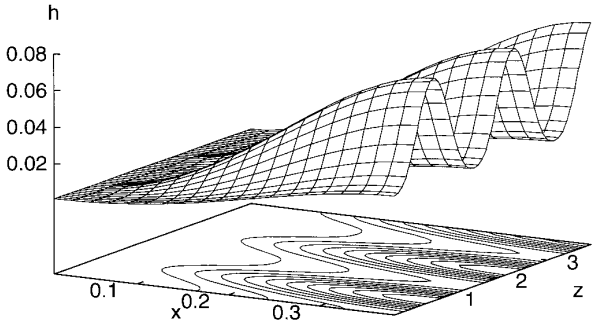

FIG. 18. Surface plot of h versus x and z, with contours, for the $R_c = 0.125$ case at $t = 1400$. Here large-amplitude waves have formed on the bottom half of the cylinder, but the coating is still thin on the top of the cylinder.

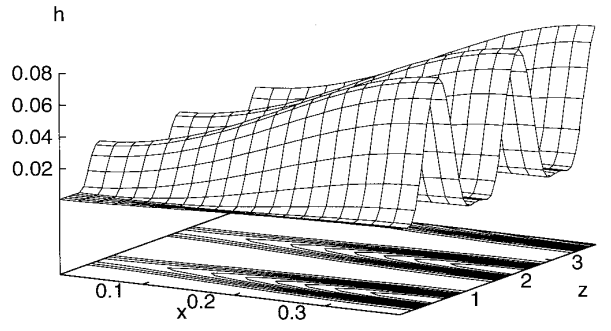

FIG. 19. Surface plot of h versus x and z, with contours, for the $R_c = 0.125$ case at $t = 1800$. Here the drops wrap around the entire circumference of the cylinder, and satellite drops are starting to form in the troughs.

$$E_\sigma + E_g + \lambda_1 V = \text{minimum}, \qquad [59]$$

where λ_1 is a Lagrange multiplier and

$$V = \iint \frac{h}{2}(2R_c + h)d\theta dz. \qquad [60]$$

Equation [59] may be written

$$\iint f(h, h_\theta, h_z)d\theta dz = \text{minimum}, \qquad [61]$$

with f given by

$$f = \cos\theta\left[\frac{(R_c + h)^3}{3} - \frac{R_c^3}{3}\right] + \sqrt{h_z^2(h + R_c)^2 + h_\theta^2 + (h + R_c)^2} + \lambda_1 \frac{h}{2}(2R_c + h). \qquad [62]$$

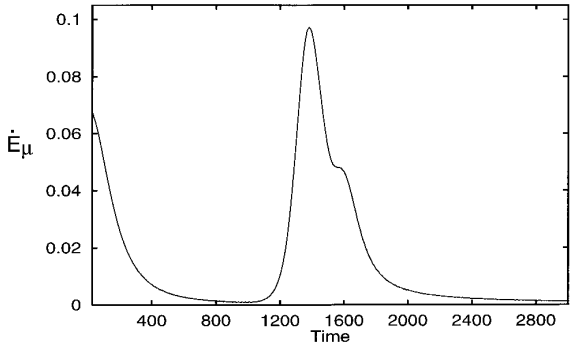

FIG. 20. Rate of energy dissipated in viscous heating, $\dot{E}_\mu = -(\dot{E}_\sigma + \dot{E}_g)$, plotted as a function of time for the $R_c = 0.125$ case. The $t \leqslant 1000$ time span represents gravity-driven drainage. For $1100 \leqslant t \leqslant 1500$, large-amplitude longitudinal waves grow to form discrete drops on the cylinder bottom, with the peak at $t \approx 1300$ representing the highest growth rate. At $t \approx 1600$, the second peak, liquid is drawn toward the top of the cylinder. For larger times, satellite drops form and the coating evolution slows as the profile moves toward steady state.

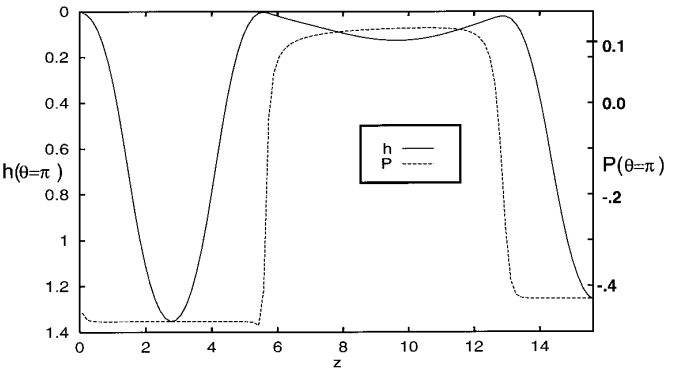

FIG. 21. Coating thickness h and pressure P corresponding to the $R_c = 1$ case at $t = 10{,}000$ shown in Fig. 8. The pressure in each drop approaches a constant when h at the pinch points between the drops approaches zero.

f is minimized when

$$\frac{\partial f}{\partial h} - \frac{\partial}{\partial \theta}\left(\frac{\partial f}{\partial h_\theta}\right) - \frac{\partial}{\partial z}\left(\frac{\partial f}{\partial h_z}\right) = 0, \qquad [63]$$

which reduces to Eq. [58] with $\lambda_1 = -C$. Consequently, a plot of the dimensionless hydrostatic pressure

$$P(\theta, z) = \kappa + (R_c + h)\cos\theta, \qquad [64]$$

should reduce to a constant when equilibrium has been reached, which corresponds to $Q^{(\theta)} = Q^{(z)} = 0$ everywhere. Thus, a check of the approach to an equilibrium state for the simulations previously presented may be obtained by plotting the function $P(\theta, z)$ at various times. Figure 21 shows a plot of $h(\theta = \pi, z)$ and $P(\theta = \pi, z)$ for the $R_c = 1$ simulation shown in Fig. 8. This figure shows that P does not reduce to a single constant along the z axis, but instead approaches a different constant in each of the three regions occupied by the two primary and one satellite drop. Because there is a sudden change in P at the ''pinch'' points between two adjacent drops, at $z = 5.5$ and $z = 13$, the pressure gradient is large here, but h^3 is very small in these regions, allowing only a small flux from the satellite drops to the primary drops. At steady state the coating thickness at these pinch points is exactly zero, and the drops cease to communicate with each other. At this final stage, the slope of the free surface at the pinch point may still be continuous, but there will in general be a discontinuity in κ, and therefore in P, when $h = 0$ at the pinch points and the flux here, and everywhere else in the drop, is zero. The surface and contour plot of $P(x, z)$ in Fig. 22 shows that $P(x, z)$ approaches a constant value for each drop not only along the plane $\theta = \pi$, but everywhere in the (x, z) domain occupied by each drop.

The approach to this equilibrium state for $R_c = 0.125$, corresponding to the same simulation shown in Fig. 15, is shown in Fig. 23. Here $P(\theta = \pi, z)$ is uniform before the growth of discrete drops, but evolves toward a square-wave

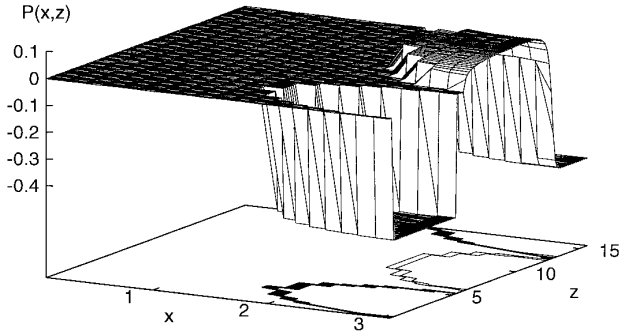

FIG. 22. Surface and contour plot of $P(x, z)$ corresponding to the $R_c = 1$ case at $t = 10{,}000$ shown in Fig. 8. The pressure in each region occupied by the three drops is approximately constant.

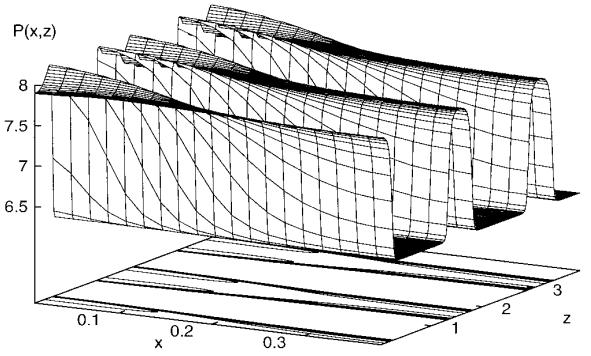

FIG. 24. Surface and contour plot of $P(x, z)$ for the $R_c = 0.125$ case at $t = 3000$ shown in Fig. 15. The pressure in each region occupied by the drops is approximately constant.

pattern as three primary drops and three satellite drops form between $t = 1000$ and $t = 3000$. A surface and contour plot for this same case is shown in Fig. 24, demonstrating that P approaches a constant value everywhere in the (x, z) domain occupied by each of the three primary drops and three satellite drops.

B. Static Drops

In the last section we simulated the formation and evolution of small-amplitude drops using the numerical technique developed in Section III. In this section, we use the same technique to determine equilibrium shapes for large drops when there is an exact balance between surface tension and gravitational forces. The shape of such drops can be obtained by starting with an initial volume and running the simulation for a given R_c until steady state has been reached by the criteria considered in the last section. For drops of large fluid volume, the small-slope requirement is not uniformly satisfied; thus evolving profiles are not time accurate. As a method for finding equilibrium solutions, however, it is competitive with the Newton iteration approach of Lawal and Brown (22), for example. Unlike Newton iteration, the present quasi-time-dependent method also verifies stability, at least within the dynamical modes included in the small-slope approximation.

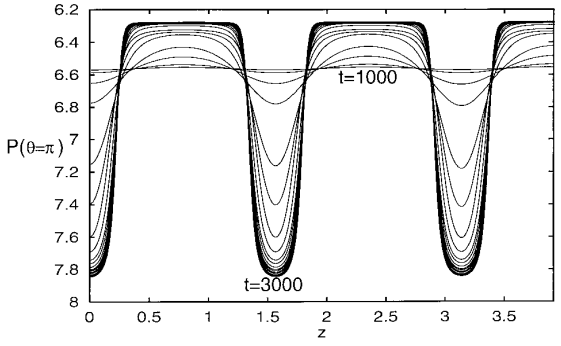

FIG. 23. Time evolution of $P(\theta = \pi, z)$ for the $R_c = 0.125$ case shown in Fig. 15. The pressure approaches a constant in each drop with a discontinuity at the borders between adjacent drops.

Figures 25 and 26 show a perspective view of large-amplitude drops on cylinders of various radii. The figures were produced by starting with an initial volume and running the simulation for a given nondimensional cylinder radius R_c until $P(\theta, z)$ varied by no more than 1% over the region occupied by the drop. The volume of the drop was then increased and the simulation continued until $P(\theta, z)$ stabilized again. If $P(\theta, z)$ did not stabilize, the volume was reduced. At each iteration, the cylinder length Z_{max} in the computational domain was adjusted so that there were a sufficient number of extra nodes to the right of the last node occupied by the drop so that the imposed boundary conditions of $Q(z = Z_{max}, \theta) = 0$, $h_z\,(z = Z_{max}, \theta) = 0$ did

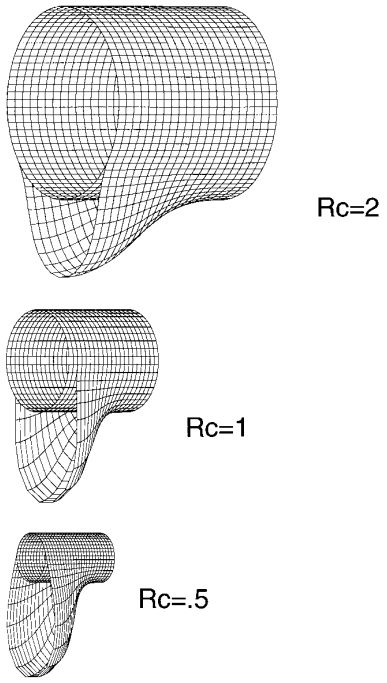

FIG. 25. One-half of a bilaterally symmetric drop corresponding to the maximum sustainable volume for cylinders of radius $R_c = 2$, $R_c = 1$, and $R_c = 0.5$. Note that the plots are viewed at an angle of 55° with respect to the z axis.

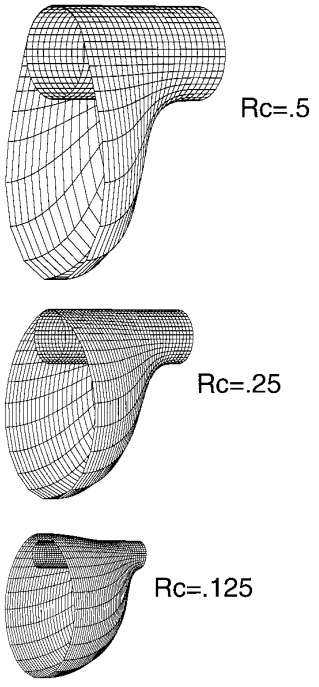

FIG. 26. One-half of a bilaterally symmetric drop corresponding to the maximum sustainable volume for cylinders of radius $R_c = 0.5$, $R_c = 0.25$, and $R_c = 0.125$.

not affect the drop shape when additional volume was added to the drop. In effect, the drop found its own length, and in drawing the plots shown in Figs. 25 and 26, the extra nodes in the computational domain, all with negligible h, were not shown. Using this iterative scheme, the maximum volume for drops on cylinders of various radii was obtained.

The final drop shapes for cylinders of various radii are shown in Figs. 25 and 26. Here we view a cut section of the drop and supporting cylinder at an angle of 55° with respect to the z axis. Note in particular the $R_c = 0.125$ case, where a substantial portion of the drop remains above the top surface of the cylinder, forming a part sessile, part pendant drop. The maximum volume a given cylinder can support increases with increasing cylinder radius. This function is plotted in Fig. 27, with the volume in units of l_c^3 and R_c in units of l_c. A drop on a cylinder of infinite radius would correspond to a static axisymmetric drop on a horizontal substrate, and the maximum volume for such a drop is included for reference in the figure. Consequently we expect the maximum drop volume to asymptotically approach this value for large R_c. The three data points at the low end of the spectrum in Fig. 27 require a more detailed explanation. Figure 28 shows profile views for maximum volume drops on cylinder radii of $R_c = 0.125$, $R_c = 0.05$, and $R_c = 0.01$. As R_c decreases the drop profiles become more symmetric with respect to the z axis as surface tension forces become stronger than gravitational forces. For the $R_c = 0.01$ case we also plot the axisymmetric result for comparison. [The axisymmetric result was produced by matching the radius

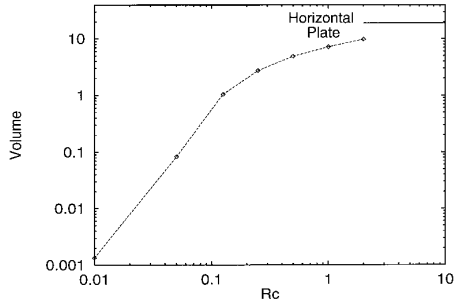

FIG. 27. Maximum sustainable drop volume on a cylinder versus cylinder radius. The drop volumes are in units of l_c^3 and cylinder radii are in units of l_c. The maximum sustainable volume on a horizontal substrate, corresponding to an infinite cylinder radius, is also shown.

and wavelength from the numerical result with the two free parameters allowed in the axisymmetric solution (25).] Note that though the drop profiles approach the axisymmetric case for small R_c, we cannot use the axisymmetric results alone to predict the maximum drop volume. This is due to the fact that the effect of gravity is not only to remove the axisymmetry in the drop shape, but also to enforce a wavelength for the resultant drop. There is no maximum drop volume for the axisymmetric case, for here the amplitude increases monotonically with the wavelength of the drop, and drops of arbitrarily large volume may be produced by simply increasing the wavelength. The results given in Fig. 27 may

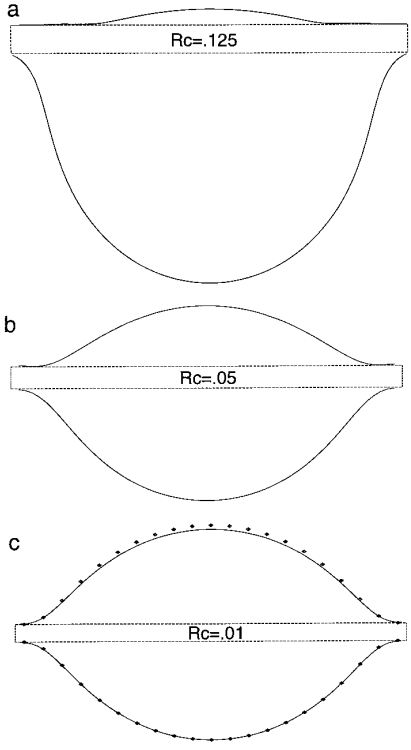

FIG. 28. Profile view of maximum volume drops on cylinders of various nondimensional radii. The symbols in the $R_c = 0.01$ case in plot c represent the profile for the axisymmetric case.

be of practical importance in applications where it is important to maximize or minimize the condensation or coating volume on cylindrical bodies such as fibers, wires, and tubes. Additionally, the static shape of drops in simple geometries can be used to predict the value of the surface tension (28). The present results can be used for the same purpose in this more complicated geometry. Such a capability may find application in certain industrial processes where noninvasive measurement is desirable.

V. CONCLUSIONS

We have derived the leading order lubrication approximation for the three-dimensional, unsteady evolution of a thin liquid film on a horizontal right circular cylinder. The resultant equations were discretized and solved numerically using an ADI technique. The resulting algorithm is computationally efficient and allows the modeling of coating evolutions over a wide range of cylinder radii.

Simulations show that the transition from a uniform coating to a pattern of distinct drops follows a similar evolution for a wide range of cylinder radii. Initially gravity-driven drainage from the top and sides of the cylinder damps the formation of any axial disturbances, and only when this drainage slows do longitudinal waves begin to grow along the bottom of the cylinder. These waves grow rapidly and a series of alternating primary and satellite drops form during the transition from linear to nonlinear wave growth regimes. This is followed by a slow drainage between adjacent drops as the drop pattern approaches an equilibrium state where surface tension forces exactly balance gravitational forces in each discrete drop. For large cylinder radii, the drops are localized on the bottom of the cylinder, while for sufficiently small cylinder radii these drops may wrap around the entire circumference of the cylinder, forming part sessile, part pendant drops. Integral measures of the evolving coating profile, such as the total energy and viscous dissipation rate, clearly show these growth phases. These energy-versus-time plots identify time scales for slow forming events, such as gravity-driven drainage, and more rapid events, such as drop formation. Such distinct time scales seem to be a property of many capillary-dominated flows. The equilibrium state of each drop, where surface tension exactly balances gravity, is shown to correspond to a minimum in the total potential energy subject to the constraint of constant volume, and this relation is used to evaluate the approach to equilibrium.

By employing the exact expression for the radius of curvature of the free surface, which is somewhat more difficult to implement but no more computationally intensive compared with the small-slope approximation, we have also been able to predict the final equilibrium shape of large-amplitude pendant drops on cylinders of various radii. For these cases, the time-dependent algorithm is run until the effects of viscous forces are negligible, and the final drop profile corresponds closely to the equilibrium state for a pendant drop on a prewetted horizontal circular cylinder. Such a method will fail to find a stable drop profile only when the drop volume for a given cylinder radius is too large, and this fact was used to determine the maximum drop volume a given cylinder may support.

Applications of this work include the coating of wires, fibers, and tubes, as well as the condensation on ducts and condenser tubes used in most refrigeration and air-conditioning machinery. Results are relevant to both normal and low-gravity environments.

ACKNOWLEDGMENTS

This work was supported by the ICI Strategic Research Fund, the State of Delaware, and the NASA Microgravity Program.

REFERENCES

1. Schwartz, L. W., *Phys. Fluids A* **1,** 443 (1989).
2. Chang, H. C., *in* ''Annual Review of Fluid Mechanics'' (J. Lumley, M. Van Dyke, and H. Reed, Eds.), pp. 103–136. Annual Reviews, Palo Alto, CA, 1994.
3. Rayleigh, W. S., ''Scientific Papers.'' Cambridge Univ. Press, Cambridge, England, 1902.
4. Goren, S. L., *J. Fluid. Mech.* **12,** 309 (1962).
5. Hammon, P. S., *J. Fluid. Mech.* **137,** 363 (1983).
6. Gauglitz, P. A., and Radke, C. J., *Chem. Eng. Sci.* **43,** 1457 (1988).
7. Mashayek, F., and Ashgriz, N., *Phys. Fluids* **7**(9), 2143 (1995).
8. Lin, S. P., and Liu, W. C., *AIChE J.* **21**(4), 775 (1975).
9. Atherton, R. W., and Homsy, G. M., *Chem. Eng. Commun.* **2,** 57 (1976).
10. Krantz, W. B., and Zollars, R. L., *AIChE J.* **22,** 930 (1976).
11. Shlang, T., and Sivashinsky, G. I., *J. Phys. Paris* **43,** 145 (1982).
12. Solorio, F. J., and Shen, M. C., *J. Fluid. Mech.* **183,** 365 (1987).
13. Moffatt, H. K., *J. Fluid. Mech.* **16,** 651 (1977).
14. Preziosi, L., and Joseph, D. D., *J. Fluid. Mech.* **187,** 99 (1988).
15. Hansen, E. B., and Kelmanson, M. A., *J. Fluid. Mech.* **272,** 91 (1994).
16. Dávalos-Orozco, L. A., and Ruiz-Chavarría, G., *Phys. Fluids A* **5,** 2390 (1993).
17. Schwartz, L. W., and Weidner, D. E., *J. Eng. Math.* **29,** 91 (1995).
18. Weidner, D. E., Schwartz, L. W., and Eley, R. R., *J. Colloid Interface Sci.* **179,** 66 (1996).
19. Bashforth, F., and Adams, J. C., ''The Theories of Capillary Action.'' Cambridge Univ. Press, Cambridge, England, 1883.
20. Hartland, S., and Hartley, R. W., ''Axisymmetric Fluid Interfaces.'' Elsevier, New York, 1976.
21. O'Brien, S. B. G., *J. Fluid. Mech.* **233,** 519 (1991).
22. Lawal, A., and Brown, R. A., *J. Colloid Interface Sci.* **89,** 322 (1982).
23. Benney, B. J., *J. Math. Phys.* **45,** 150 (1966).
24. Conte, S. D., and Dames, R. T., *Math. Tables Aids Comput.* **12,** 198 (1958).
25. Princen, H. M., *in* ''Surface and Colloid Science'' (E. Matijeric and F. Eirich, Eds.), Vol. II, pp. 1–84. Interscience, New York, 1969.
26. Joseph, D. D., and Preziosi, L., *J. Fluid. Mech.* **185,** 323 (1987).
27. Yiantsios, S. G., and Higgins, B. J., *Phys. Fluids A* **9,** 1484 (1989).
28. Anastasiadis, S. H., Chen, J. C., Koberstein, J. T., Sohn, J. E., and Emerson, J. A., *J. Colloid Interface Sci.* **119,** 55 (1987).